Scilight

Power Electronics Research and Applications Transactions
https://www.sciltp.com/journals/perat



Check for updates

Article

High-Conversion-Ratio Bidirectional DC–DC Converter Derived from Gain Cells: Analysis and Experimental Validation

Tiago P. Metzger [1,*,†], Guilherme Bauer [1,†], Bruno Benedetti [1,†], Luis H. D. Sismeiro [1,†], Mateus N. Mezaroba [1,†], Neilor C. Dal Pont [1,†], Antonio L. S. Pacheco [1,†], Jéssika M. de Andrade [2,†] and Telles B. Lazzarin [1,†]

[1] Department of Electrical Engineering, Federal University of Santa Catarina, Florianópolis 88040-900, Brazil
[2] Department of Mobility Engineering, Federal University of Santa Catarina, Joinville 89219-600, Brazil
* Correspondence: tiago.peron.metzger@gmail.com
† These authors contributed equally to this work.

How To Cite: Metzger, T.P.; Bauer, G.; Benedetti, B.; et al. High-Conversion-Ratio Bidirectional DC–DC Converter Derived from Gain Cells: Analysis and Experimental Validation. *Power Electronics Research and Applications Transactions* **2026**. https://doi.org/10.53941/perat.2026.100012

Received: 3 September 2026
Revised: 23 September 2026
Accepted: 28 September 2026
Published: 10 October 2026

Abstract: Emerging applications such as energy-storage systems, electric vehicles, and data centers increasingly require bidirectional DC–DC converters capable of providing high conversion ratios between widely different voltage levels. Although switched-inductor and voltage-multiplier cells have been extensively employed in unidirectional high-step-up converters, extending these cells to bidirectional operation is not straightforward. This paper addresses these challenges and proposes a non-isolated high-conversion-ratio bidirectional converter that combines an active switched-inductor cell with an active switched-voltage-multiplier cell. Its operating states, static voltage gains, component stresses, dynamic models, and closed-loop control are analyzed. A 300 W prototype operating between 380 V and 48 V is developed and evaluated under open- and closed-loop conditions. The experimental results validate the theoretical analysis and bidirectional operation, demonstrating peak efficiencies of 97.0% in buck mode, from 380 V to 48 V, and 96.1% in boost mode, from 48 V to 380 V.

Keywords: bidirectional; dc–dc; high conversion ratio

1. Introduction

The growing demand for computational resources, driven by technological advances such as artificial intelligence, 5G networks, energy storage systems, electric vehicles, and data centers, has considerably increased the power requirements of modern computing infrastructure [1–5]. In 2024, data centers consumed approximately 415 TWh of electricity worldwide, corresponding to about 1.5% of global electricity consumption [6]. This trend has intensified the need for efficient power-conversion architectures capable of reducing distribution losses and the associated energy consumption.

These facilities adopt distribution systems with typical voltage levels ranging from 240 to 380 VDC in order to minimize conduction losses, while the supplied equipment usually operates at very low-voltage levels, often ranging from 12 V down to 1 V. To bridge this gap, a multi-stage power conversion architecture is commonly employed, using a 48 V bus. Figure 1a shows a conventional low-voltage power distribution structure used in telecommunications facilities and data centers [7]. Meanwhile, Figure 1b illustrates the 48 V rack architecture adopted by Google, in which a bidirectional DC–DC converter interfaces the 380 V bus with a 48 V battery system [8]. During normal operation, the converter charges the uninterruptible power supply batteries, whereas during a grid outage it reverses the power flow to supply the DC bus [8]. In this architecture, galvanic isolation is not inherently required in the 380 V/48 V conversion stage because the high-voltage DC bus and the battery system are part of the same DC power distribution domain, and the converter is not intended to provide electrical separation

Copyright: © 2026 by the authors. This is an open access article under the terms and conditions of the Creative Commons Attribution (CC BY) license (https://creativecommons.org/licenses/by/4.0/).
Publisher's Note: Scilight stays neutral with regard to jurisdictional claims in published maps and institutional affiliations.

between the source and the load. Consequently, a non-isolated high-conversion-ratio DC–DC converter can be employed to accommodate the large voltage conversion ratio while avoiding the additional losses, volume, and complexity associated with a high-frequency isolation transformer

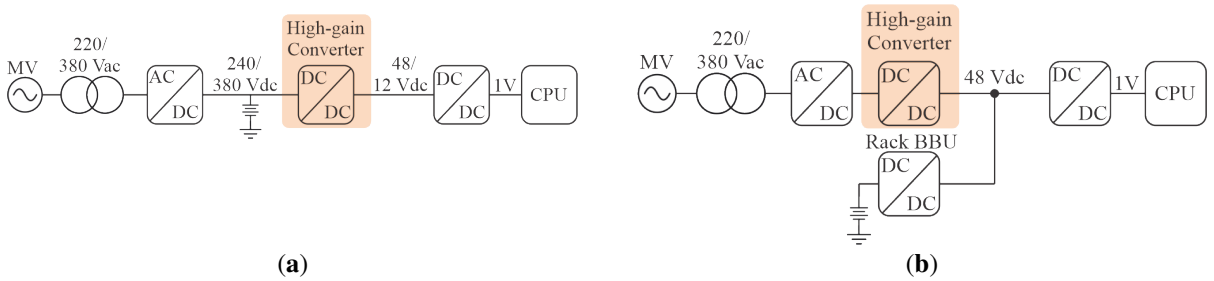


Figure 1. Data center power supply systems: (**a**) conventional LVDC architecture [7]; (**b**) Google 48 VDC architecture [8].

Achieving efficient conversion from 380 V down to 48 V remains challenging for conventional converter topologies. Although the conventional bidirectional buck converter offers a simple structure, this step-down operation requires a very low duty cycle, which can increase current stress and conduction losses [9,10]. Another very conventional option for conversion between these voltage levels in this type of application is the use of resonant LLC converters [11–16]; however, for this type of topology it is necessary to employ a transformer, which is not always desirable since this component increases the volume and weight of the converter [9]. Another desirable characteristic in these applications is bidirectionality, in order to enable integration of the 48 V bus with a battery bank [8,17]. Consequently, alternative topologies with high voltage conversion capability, non-isolated, bidirectional, and with high efficiency have become an important focus of research.

One potential approach to achieving high conversion ratios in bidirectional DC–DC converters is the use of voltage-gain cells, which are circuit building blocks incorporated into conventional converter topologies to extend their static conversion ratios [18]. Switched-inductor and voltage-multiplier cells have been widely investigated in unidirectional high-step-up converters [18–23]. Nevertheless, extending these cells to bidirectional power conversion is not necessarily straightforward. In addition to replacing their diodes with controllable switches, the reverse power-flow path, switching states, voltage gain (as step-down and step-up), component stresses, and control behavior must be established for both operating directions. Therefore, the derivation and validation of bidirectional converters from gain cells originally conceived for unidirectional operation remain relevant topics of investigation [24,25].

Relevant developments in this field include the switched-capacitor and switched-inductor structures reported by [26], which established building blocks for transformerless hybrid DC–DC conversion. Bidirectional hybrid switched-capacitor architectures were subsequently investigated for dual-voltage automotive systems in [27], while [28] explored a non-isolated three-level bidirectional converter combining interleaved conversion and a switched-capacitor network. Further developments include the family of hybrid converters derived from an active switched-capacitor commutation cell in [29] and the cascade/ladder switched-capacitor architecture combined with an interleaved synchronous buck stage in [30]. Although not all these studies experimentally demonstrate bidirectional operation, they provide relevant foundations for evaluating voltage-gain cells, semiconductor stresses, and component requirements. Together, these contributions place the present work within the development of non-isolated gain-cell-based converters, with emphasis on the bidirectional adaptation and validation of the selected ASL–ASVMC combination. It is also important to note that extending a unidirectional converter to bidirectional operation is not limited to replacing diodes with controllable switches. Such an adaptation introduces additional design challenges, including the development of appropriate gate-drive and switching strategies, the definition of the voltage-gain characteristics in both power-flow directions, the derivation of suitable models for each operating mode, and the design and validation of control strategies capable of ensuring stable operation under bidirectional power transfer. Despite the progress reported in the literature, the systematic migration of non-isolated gain-cell-based converters from unidirectional to bidirectional operation remains comparatively underexplored. In this context, the present work contributes to this development by investigating the bidirectional adaptation of the selected ASL–ASVMC combination [24,25].

In this context, this paper investigates the bidirectional adaptation of unidirectional voltage gain cells and demonstrates the resulting derivation process through a high-conversion-ratio DC–DC converter as a case study. The main contributions include a comparative analysis of representative switched-inductor and voltage-multiplier cells, followed by the derivation of a non-isolated bidirectional converter that combines an active switched-voltage-multiplier cell with a switched-inductor cell. The static and dynamic models of the proposed converter are developed for both power-flow directions. Experimental validation is performed using a 300 W prototype operating between

380 V and 48 V, with open-loop and closed-loop operation as well as efficiency results presented. Finally, the proposed converter is compared with other bidirectional high-conversion-ratio topologies reported in the literature.

2. From Unidirectional Gain Cells to Bidirectional DC–DC Converters

2.1. Voltage Gain Cells

In the study of dc–dc step-down converters, the buck topology stands out as one of the simplest, since it employs only one switch, one diode, one inductor and one capacitor. The converter is illustrated in Figure 2a. In addition, another dc–dc topology that stands out for its simplicity is the boost converter, which has the same number of components as the buck converter; however, it is used to increase the input voltage. This converter is illustrated in Figure 2b.

The buck converter topology can also be modified by replacing the diode with another switch and placing another voltage source on the high-voltage side, thus obtaining a bidirectional topology capable of processing power both with the current flowing from the high-voltage side to the low-voltage side and vice versa. The gating signal of switch S_2 is complementary to that of switch S_1. It is also worth noting that, when analyzing the bidirectional buck converter, the input seen from the load side exhibits boost behavior. Similarly, in the bidirectional version of the boost converter, the input seen from the load side exhibits buck behavior. The topology of the bidirectional buck converter is shown in Figure 2c.

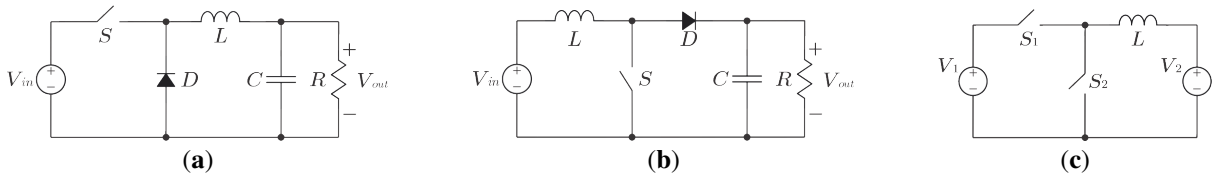


Figure 2. Basic converters: (**a**) buck converter; (**b**) boost converter; (**c**) bidirectional buck converter.

Despite the simplicity of the bidirectional buck converter, it exhibits the same drawbacks as the traditional buck converter previously mentioned. An alternative of great interest for applications with high conversion ratios is the use of gain cells, which are circuit blocks that can be inserted to increase the voltage gain of a given topology [18]. Figure 3a–c generically illustrate the insertion of switched-inductor gain cells (A-SL), voltage multiplier cells (VMC), as well as their cascaded connection within a circuit.

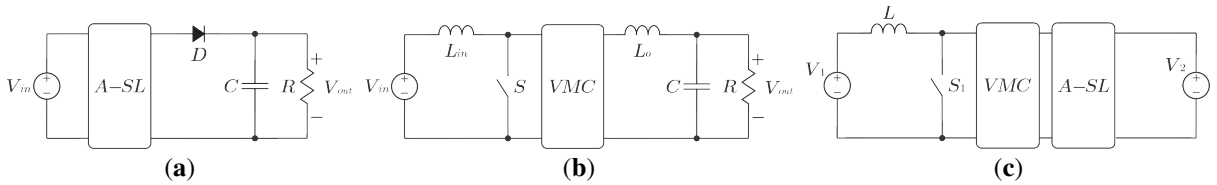


Figure 3. General voltage gain cells: (**a**) active switched-inductor cell (A-SL); (**b**) voltage multiplier cell (VMC); (**c**) cascaded cells.

Both cells presented in Figure 3 operate in a very similar manner, in which one or more passive elements (inductors in the case of the ASL cell and capacitors in the case of the VMC cell) store energy during one operating stage and, subsequently, in the second stage, are connected in series with the circuit, thereby providing an increase in the voltage levels. The switched-inductor cell is shown in Figure 4a, and the voltage multiplier cell is shown in Figure 4b.



Figure 4. Voltage gain cells: (**a**) active switched-inductor cell; (**b**) voltage multiplier cell.

Notably several switched-inductor and voltage-multiplier cells have been reported in the literature [18] as unidirectional cells. Representative structures are shown in Figure 5, and their main characteristics are summarized in Table 1, including the ideal voltage gain and the required numbers of passive elements, switches, and diodes [18].

Table 1. Characteristics of different gain cells.

Topology	Voltage Gain	No. of Passive Elements	No. of Switches	No. of Diodes
Figure 4a	$\frac{1+D}{1-D}$	2 inductors	2	0
Figure 5a	$\frac{3-D}{1-D}$	2 inductors & 2 capacitors	2	2
Figure 5b	$\frac{1+3D}{1-D}$	4 inductors	2	6
Figure 4b	$\frac{1+D}{1-D}$	2 capacitors	0	2
Figure 5c	$\frac{1+D}{1-D}$	2 capacitors	0	2
Figure 5d	$\frac{1+D}{1-D}$	2 capacitors & 1 inductor	0	2

For the switched-inductor structures, the cells shown in Figure 5a,b provide higher voltage gains than the basic ASL cell in Figure 4a, at the expense of additional components [19,20]. The voltage-multiplier cells shown in Figure 4b and Figure 5c have the same ideal voltage gain but provide non-inverting and inverting output voltages, respectively [21]. The cell shown in Figure 5d requires an additional inductor but can provide zero-current switching, increased voltage gain, and reduced reverse-voltage stress across its diodes [22].

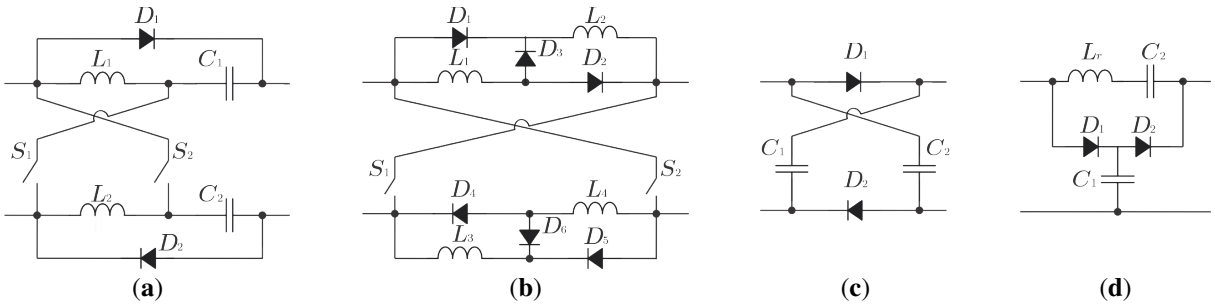


Figure 5. Voltage gain cells: (**a**,**b**) active switched-inductor cells; (**c**,**d**) voltage multiplier cells.

2.2. High-Conversion-Ratio Converters Derived from Gain Cells

Several topologies based on voltage-gain cells have been proposed in the literature to achieve high voltage conversion ratios [19–22]. Among these solutions, the converter presented in [23] is particularly relevant to the present study because it combines the basic ASL and VMC structures presented in Figure 3. Its topology, shown in Figure 6 provides a suitable starting point for investigating how a high-step-up converter originally developed for unidirectional operation can be extended to bidirectional power flow.

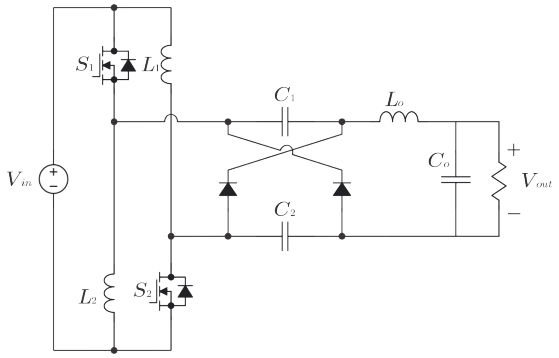


Figure 6. Converter presented in [23].

2.3. Bidirectional Extension of Voltage Gain Cells

Extending a voltage gain cell to bidirectional operation requires establishing valid current paths and switching states for both power-flow directions. For cells containing diodes, this process generally involves replacing the unidirectional devices with controllable switches. However, this replacement alone is not sufficient to characterize bidirectional operation. The switching functions, reverse power-flow paths, static voltage gains, voltage and current stresses must also be determined for both operating directions. Consequently, the resulting bidirectional topology cannot simply be treated as the original unidirectional converter operating in reverse. The step-up and step-down voltage gains, component stresses, input and output characteristics must be reassessed, including the continuity of the port currents and the required inductive or capacitive filtering. Moreover, reversing the power flow may result in different dynamic models and control-to-output transfer functions, requiring the control system to be designed according to the operating direction and the variable controlled at each port [24,25].

The bidirectional operation of all gain-cell structures presented in Table 1 is analyzed, and their ideal static voltage gains in both boost (step-up) and buck (step-down) modes are summarized in Table 2, together with their required numbers of passive elements and controllable switches. In this analysis, D denotes the duty cycle used in boost mode, whereas $D' = 1 - D$ denotes the complementary duty cycle adopted in buck mode.

This comparison shows that extending gain cells to bidirectional operation may significantly increase the required number of controllable switches, particularly for structures originally containing several diodes. Therefore, voltage gain must be considered together with component count and implementation complexity when selecting cells for a bidirectional converter. Based on this tradeoff, the basic ASL and VMC structures are selected and combined in the following section to derive the proposed high-conversion-ratio bidirectional converter.

Table 2. Characteristics of different bidirectional gain cells.

Topology	Boost Gain	Buck Gain	No. of Passive Elements	No. of Switches
Figure 2c	$\frac{1}{1-D'}$	D	2 inductors	2
Figure 4a	$\frac{1+D}{1-D}$	$\frac{D'}{2-D'}$	1 inductor	2
Figure 5a	$\frac{3-D}{1-D}$	$\frac{D'}{2+D'}$	2 inductors & 2 capacitors	4
Figure 5b	$\frac{1+3D}{1-D}$	$\frac{D'}{4-3D'}$	4 inductors	8
Figure 4b	$\frac{1+D}{1-D}$	$\frac{D'}{2-D'}$	2 capacitors	2
Figure 5c	$\frac{1+D}{1-D}$	$\frac{D'}{2-D'}$	2 capacitors	2
Figure 5d	$\frac{1+D}{1-D}$	$\frac{D'}{2-D'}$	2 capacitors & 1 inductor	2

3. 48 V to 380 V Bidirectional Converter Derived from Gain Cells

To demonstrate the derivation of a bidirectional DC–DC converter from unidirectional gain cells while meeting the high conversion ratio required between the 48 V and 380 V buses, the high-step-up topology introduced in [23] is selected as the starting point. As discussed in Section II, this converter is particularly suitable for this purpose because it combines the basic switched-inductor and voltage-multiplier cells. Although its unidirectional operation was analyzed in [23], a bidirectional converter derived from this particular combination of gain cells has not yet been reported. Applying the bidirectional extension discussed in Section II-C results in the converter shown in Figure 7, in which the constituent gain cells are highlighted.

The resulting topology combines an active switched-inductor (ASL) cell with an active switched-voltage-multiplier cell (ASVMC). The switched-capacitor cell formed by C_1, C_2, S_1, and S_2 is based on the structure previously reported in [26]. The controllable switches of the ASVMC establish the current paths required for reverse power flow while preserving the high conversion ratio provided by the original combination of gain cells. The converter operates in buck mode when power flows from the high-voltage side V_1 to the low-voltage side V_2, and in boost mode when the power-flow direction is reversed. The following subsections present its operating states, static voltage gain, component stresses, and dynamic model.

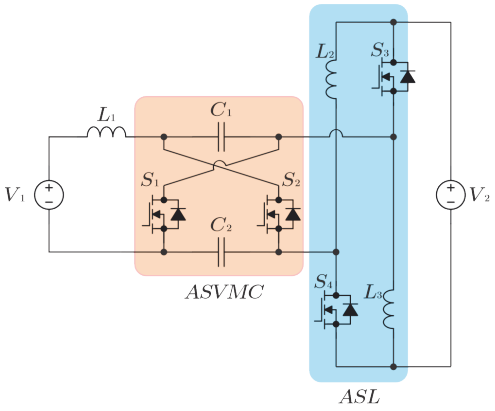


Figure 7. Proposed converter.

The proposed converter does not share a common ground between its ports; therefore, their negative terminals must not be directly connected. Practical integration requires a compatible grounding arrangement, such as a battery power circuit floating relative to the high-voltage-bus return, with isolated sensing, gate-drive, and communication interfaces where needed to prevent unintended ground connections. Switching-induced common-mode currents through parasitic capacitances can be mitigated by minimizing high-dv/dt copper areas and coupling to chassis, controlling switching slew rates, and implementing common-mode filtering suited to the installation. These measures do not provide galvanic isolation between the power ports. Common-mode emissions and mitigation effectiveness were not experimentally evaluated in this work.

3.1. Topological States

The proposed converter operates through two topological states during each switching period, as illustrated in Figure 8a,b.

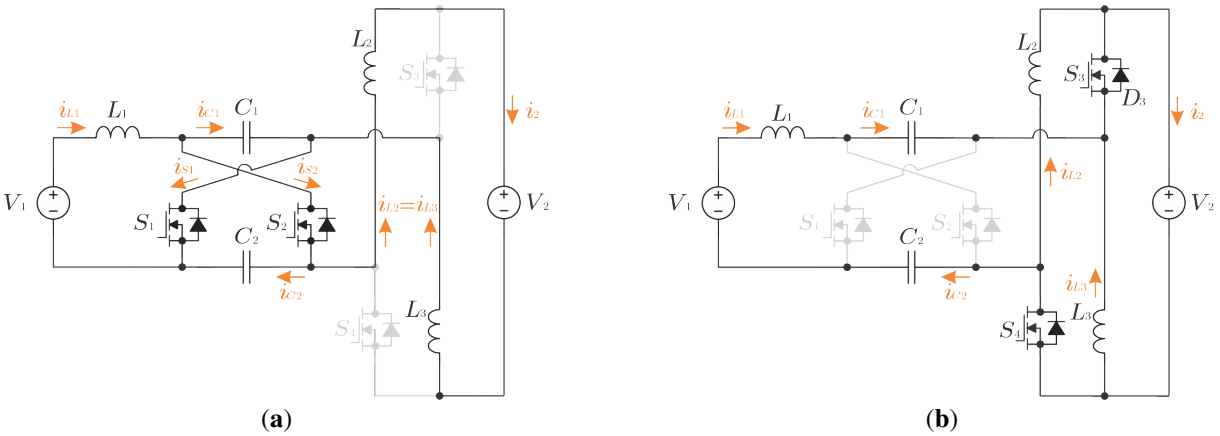


Figure 8. Topological states of the proposed converter: (**a**) first topological state; (**b**) second topological state.

- First topological stage: In this first stage, switches S_1 and S_2 are conducting, while switches S_3 and S_4 are in the blocking state, which causes capacitors C_1 and C_2 to be charged being connected in series with inductor L_1 and in parallel with each other. Inductors L_2 and L_3 are connected in series with the low side voltage, supplying energy to the load; thus, the following equations are obtained:

$$V_{L1} = V_1 - V_C \tag{1}$$

$$V_L = V_{L2} = V_{L3} = \frac{V_C - V_2}{2}. \tag{2}$$

- Second operating stage: In the second stage, switches S_1 and S_2 enter the blocking state and switches S_3 and S_4 enter conduction, which causes capacitors C_1 and C_2 to be discharged while connected in series, charging inductors L_2 and L_3 while also supplying energy to the load. Thus, the following equations can be derived:

$$V_{L1} = V_2 + 2V_C - V_1 \tag{3}$$

$$V_L = V_{L2} = V_{L3} = -V_2. \tag{4}$$

The preceding analysis assumes ideal switching transitions. In practice, a short dead time should be introduced between the gating signals of the two complementary switch pairs to prevent switching overlap and the unintended simultaneous conduction of all four switches.

3.2. Gain Analysis

For a converter operating in steady state, the average voltage across the inductors over one switching cycle must be equal to zero:

$$\int_0^{T_s} V_L dt = 0. \tag{5}$$

Therefore, this property can be used to analyze the voltage across the converter inductors. First, for the input inductor:

$$(V_1 - V_C)D + (V_2 + 2V_C - V_1)(1 - D) = 0. \tag{6}$$

As for the inductors on the ASL cell:

$$\left(\frac{V_C - V_2}{2}\right) D - V_2(1 - D) = 0. \tag{7}$$

Solving (7) for the capacitor voltage Vc is:

$$V_C = V_2 \frac{2 - D}{D}. \tag{8}$$

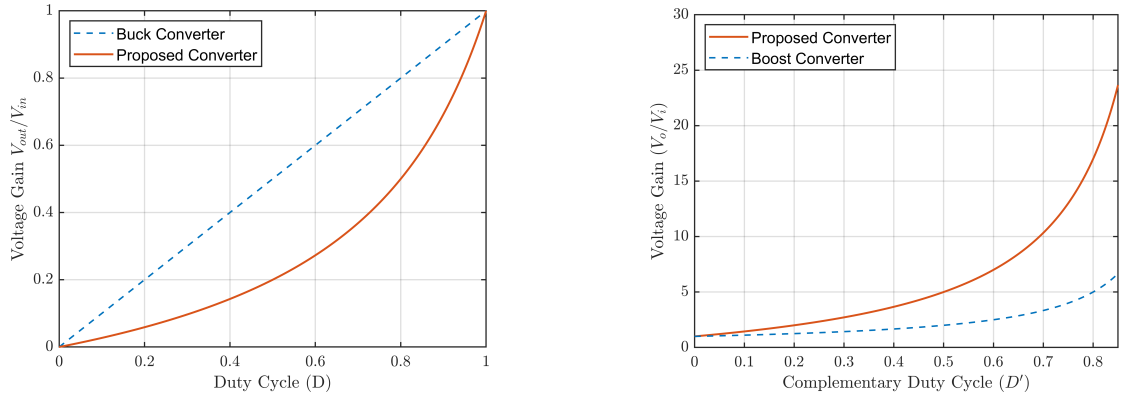
By substituting into (6), the converter gain in step-down operation is obtained:

$$G_{buck} = \frac{V_2}{V_1} = \frac{D}{4 - 3D}. \tag{9}$$

To obtain the gain of the converter operating in boost mode, a similar analysis can be performed, leading to the gain equation as a function of the complementary duty cycle:

$$G_{boost} = \frac{V_1}{V_2} = \frac{1 + 3D'}{1 - D'}. \tag{10}$$

Figure 9a shows a comparison of the gain of the proposed converter operating in step-down mode with the traditional buck converter, where it can be observed that, over the entire duty-cycle range, the proposed converter exhibits agreater step-down capability. Similarly, Figure 9b presents a comparison of the proposed converter operating in boost mode with the traditional boost converter.



(a) **(b)**

Figure 9. Comparison of the proposed converter with classical topologies: (**a**) step-down comparison with the buck converter; (**b**) step-up comparison with the boost converter.

3.3. Design Equations and Component Stresses

In order to obtain the voltage across the input inductor, Equation (8) can be substituted into (1), thus obtaining:

$$L_1 = V_1 \left(\frac{2 - 2D}{4 - 3D}\right) \frac{D}{\Delta I_1 f_s}. \tag{11}$$

The average input inductor current is the same as the average input current:

$$\overline{I_{L1}} = \overline{I_1} = \frac{P_o}{V_1}. \tag{12}$$

For the output inductors L_2 and L_3, a similar procedure is applied, in which the voltage across them is equal to the output voltage, thus yielding the equation for sizing the inductance:

$$L_{2,3} = \frac{V_2(1-D)}{\Delta I_{L2,3} f_s} = \frac{V_1 D}{4-3D}\frac{1-D}{\Delta I_{L2,3} f_s}. \tag{13}$$

The average current on the inductors $L_{2,3}$:

$$I_L = \frac{I_1(2-D)}{D}. \tag{14}$$

To perform the analysis of the voltage ripple on capacitors C_1 and C_2, it is observed that the current through the capacitors is equal to the current in the inductor L_1 during the second operating stage; therefore:

$$C = C_1 = C_2 = \frac{P_o(1-D)}{V_1 \Delta V f_s}. \tag{15}$$

The voltage across the capacitors can be obtained from Equation (8).

A low-voltage-side capacitor C_3 used to attenuate the voltage ripple when the converter is operating in step-down mode is sized considering that its voltage is equal to the low-voltage-side voltage V_2, and that the current through the component corresponds to the current ripple of inductors L_2 and L_3.

$$C_3 = \frac{\Delta i_L D}{\Delta V_{C3} f_s} \tag{16}$$

$$i_{C3\_RMS} = \sqrt{\frac{\Delta i_L^2}{12}}. \tag{17}$$

As for the switches S_1 and S_2, the blocking voltage and RMS current are given by:

$$V_{S1} = V_{S2} = V_2 + V_{C1,2} = V_1 \frac{2}{4-3D} \tag{18}$$

$$I_{S1\_RMS} = I_{S2\_RMS} = \frac{I_1}{\sqrt{D}}. \tag{19}$$

The voltage stresses across the switches S_3 and S_4 when they are on the blocking stage and their RMS current are given by:

$$V_{S3} = V_{S4} = V_2 + V_L = \frac{V_2}{D} \tag{20}$$

$$I_{S3\_RMS} = I_{S4\_RMS} = \frac{2I_1\sqrt{1-D}}{D}. \tag{21}$$

3.4. Dynamic Modeling

In order to implement closed-loop control of the converter, it is necessary to obtain the transfer functions that relate the desired voltage or current to the duty cycle. The equations used to obtain the voltages and currents on the high- and low-voltage sides as functions of the duty cycle are all fourth order. The equation relating the high-voltage-side voltage (22) has a second-order numerator, whereas the high-side current Equation (23), the low-side current Equation (25), and the low-voltage-side voltage Equation (24) all have third-order numerators [31,32].

$$G_{v1d}(s) = \frac{b_2 s^2 + b_1 s + b_0}{a_4 s^4 + a_3 s^3 + a_2 s^2 + a_1 s + a_0} \tag{22}$$

$$G_{i1d}(s) = \frac{d_3 s^3 + d_2 s^2 + d_1 s + d_0}{c_4 s^4 + c_3 s^3 + c_2 s^2 + c_1 s + c_0} \tag{23}$$

$$G_{v2d}(s) = \frac{f_3 s^3 + f_2 s^2 + f_1 s + f_0}{e_4 s^4 + e_3 s^3 + e_2 s^2 + e_1 s + e_0} \tag{24}$$

$$G_{i2d}(s) = \frac{h_3 s^3 + h_2 s^2 + h_1 s + h_0}{g_4 s^4 + g_3 s^3 + g_2 s^2 + g_1 s + g_0}. \tag{25}$$

The coefficients a_i, b_i, c_i, d_i, e_i, f_i, g_i, and h_i are functions of the passive-component values of the converter and its steady-state operating point, including the input voltage and duty cycle.

The coefficients in (22)–(25) depend on the converter component values and the steady-state operating point. For the frequency responses presented in Figure 10, the parameters are $L_1 = 7.7$ mH, $L_2 = L_3 = 691.23$ µH, $C_1 = C_2 = 2.2$ µF, and $C_3 = 100$ µF. The operating point corresponds to a high-side voltage of $V_1 = 380$ V, a low-side voltage of $V_2 = 48$ V, and a rated power of 300 W.

Both the analytical averaged model and the switched simulation model assume ideal components. Specifically, switch on-state resistances, inductor winding resistances, and capacitor equivalent series resistances are neglected in both models. Therefore, the comparison evaluates the agreement between the averaged and switched representations under the same idealized conditions; it does not assess the influence of parasitic elements.

Figure 10a–d present the simulation results comparing the Bode plots of the transfer functions obtained from (22)–(25) (orange curve) with the switched model of the converter (blue curve). The averaged and switched models exhibit close agreement over the analyzed frequency range.

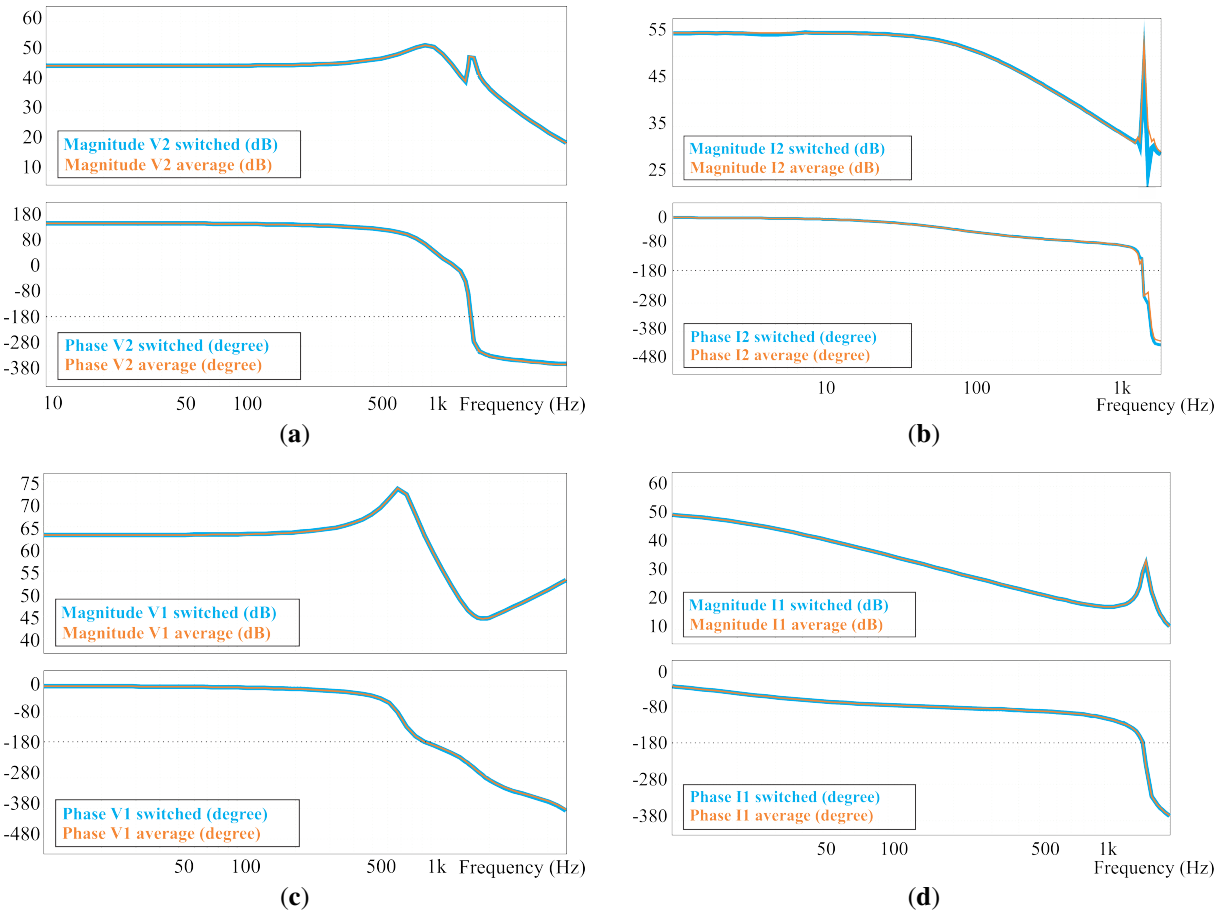


Figure 10. Small-signal frequency responses at the nominal operating point ($V_1 = 380$ V, $V_2 = 48$ V, and $P = 300$ W): (**a**) G_{v_2d}; (**b**) G_{i_2d}; (**c**) G_{v_1d}; (**d**) G_{i_1d}.

3.5. Voltage and Current PI Controller

Voltage and current regulation at either the high- or low-voltage port are common control objectives in bidirectional dc–dc converters. Accordingly, PI controllers are designed to regulate each of these variables at its corresponding reference value. Figure 11 shows a block diagram illustrating the converter control scheme, where the block $PI(s)$ represents the designed PI controller, $G_{vd/id}(s)$ denotes the voltage- or current-to-duty-cycle transfer function, and $H(s)$ represents the measurement gain of the quantities of interest. Equation (26) presents the transfer function of a PI controller, which, aiming to be implemented in a microcontroller, assumes the discrete form shown in Equation (27), where $y(k)$ is the output duty cycle, $y(k-1)$ is the duty cycle at the previous time step, $x(k)$ and $x(k-1)$ are the current and previous errors, and finally c_0 and c_1 are the controller coefficients.

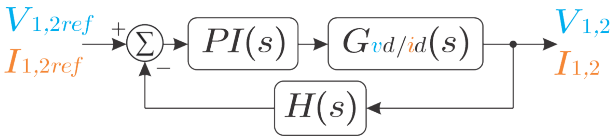


Figure 11. Controller Block Diagram.

$$C_{PI} = k_p + \frac{k_i}{s} \tag{26}$$

$$y(k) = y(k-1) + c_1 x(k) + c_0 x(k-1). \tag{27}$$

The PI controllers were designed in the continuous-time domain based on the uncompensated open-loop Bode plots of the corresponding plants. A crossover frequency of $f_c = 20$ Hz was selected below the converter's characteristic resonances, prioritizing adequate stability margins and a damped response within the phase-shaping limitations of PI controllers. This conservative choice involves a tradeoff between stability margins and transient response speed. The switching frequency of 50 kHz and sampling frequency of 100 kHz govern switching operation and digital implementation, respectively, but do not by themselves determine the control bandwidth, which also depends on the plant dynamics and compensator characteristics. The controller parameters and phase margins are summarized in Table 3.

Table 3. PI controller parameters.

Controller	f_c (Hz)	PM (°)	c_0	c_1
c_{v1}	20	120	-0.01776	0.01780
c_{v2}	20	120	-0.01737	0.01941
c_{i1}	20	90	-5.872×10^{-4}	5.905×10^{-4}
c_{i2}	20	120	-0.09396	0.09416

4. Experimental Results

Based on the aforementioned equations, a converter employing the proposed topology was designed to operate with a high-side voltage of 380 V, a low-side voltage of 48 V at a rated power of 300 W. Tables 4 and 5 depict the converter specifications and the selected components. Table 3 presents the parameters of the discrete voltage and current PI controllers designed for both the low- and high-voltage sides of the converter. The controllers were implemented using a sampling frequency of 100 kHz, with the selected crossover frequencies f_c and phase margins PM also provided in the table. Figure 12 shows the developed converter where a power density of 0.332 kW/L and power-to-weight ratio of 483.87 W/kg were obtained.

Table 4. Defined parameters for the converter.

Parameter	Defined Value
Low-side voltage	48 V
High-side voltage	380 V
Rated power	300 W
Switching frequency	50 kHz
High-side voltage current ripple	20%
Low-side voltage current ripple	25%
Voltage ripple across capacitors C_1 and C_2	2%

Table 5. Converter components.

Abbreviation	Selected Component
S_1, S_2, S_3, and S_4	C3M0065090D
C_1 and C_2	2.2 µF—RIFA PHE 840 M
L_2 and L_3	691.23 µH—IP12R E42/20 44 turns
C_3	100 µF—EPCOS B43840-A5107-M
L_1	7.7 mH—IP12R E42/20 95 turns

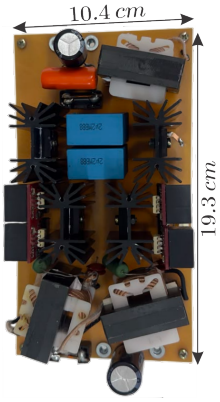


Figure 12. Developed converter.

4.0.1. Converter Waveforms

The experimental results were obtained using a MagnaPower SL 800 power supply and a Tektronix DPO 5034 oscilloscope. Figure 13 presents the measured waveforms of the converter operating in open-loop mode. The low- and high-voltage-side voltages, V_2 and V_1, were measured as 49.6 V and 379 V, respectively, while the corresponding currents, I_2 and I_1, were 5.91 A and 810 mA, respectively. These results confirm the voltage gain of the proposed converter given by (9).

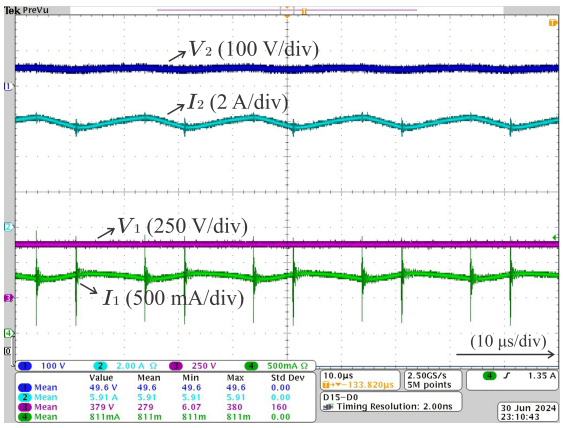


Figure 13. Step-down experimental results: low-side voltage (V_2), low-side current (I_2), high-side voltage (V_1), and high-side current (I_1).

Additionally Figure 14 corroborates the converter operating in open-loop boost mode, with the low-voltage-side voltage V_1 at 48.9 V and the high-voltage-side voltage at 376 V. In addition, the high-voltage-side current I_2 is presented with a value of 0.894 A, and the low-voltage-side current I_1 is shown with an average value of 7.13 A. Figure 15 shows the voltages across the converter switches, in which a blocking voltage of approximately 260 V can be observed across switches S_1 and S_2, and 130 V across switches S_3 and S_4, thus confirming Equations (18) and (20).

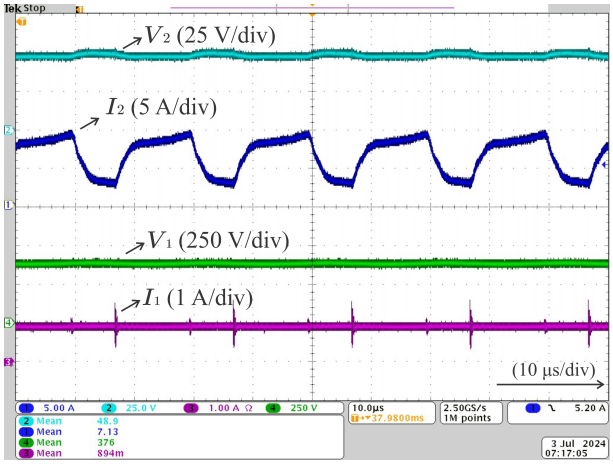


Figure 14. Step-up operation experimental results: high-side voltage (V_1), high-side current (I_1), low-side voltage (V_2), and low-side current (I_2).

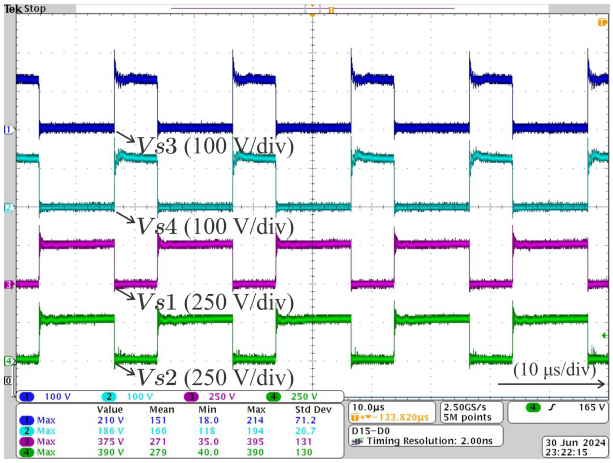


Figure 15. Voltage across switches S_1 (V_{S1}), S_2 (V_{S2}), S_3 (V_{S3}), and S_4 (V_{S4}).

4.0.2. Efficiency

In addition, the experimental results were used to evaluate the converter efficiency at different load levels and for two low-side voltage levels, 48 V and 98 V. The measurements were performed using a Yokogawa WT1800 Precision Power Analyzer, with a DC power accuracy of ±0.05%, while the converter was subjected to load steps of approximately 50 W. In step-down operation, a maximum efficiency of approximately 97% was achieved at a load of 150 W for the 380 V to 48 V voltage conversion, as shown in Figure 16a. In step-up operation, a peak efficiency of 96.08% was obtained at a load of 136.3 W for the same 48 V to 380 V voltage conversion, as shown in Figure 16b. Furthermore, the converter efficiency at rated power for different voltage gains is presented in Figure 16c,d for step-down and step-up operation, respectively.

The theoretical losses associated with the different converter components were also evaluated through simulation for the step-down and step-up modes at rated power, as shown in Figure 17a,b, respectively. The total simulated losses were 12.80 W in the step-down mode and 17.67 W in the step-up mode. It should be noted that most of the losses are concentrated in the switches, mainly due to the voltage overshoots and the current flowing through the body diode of the switches during the dead-time period.

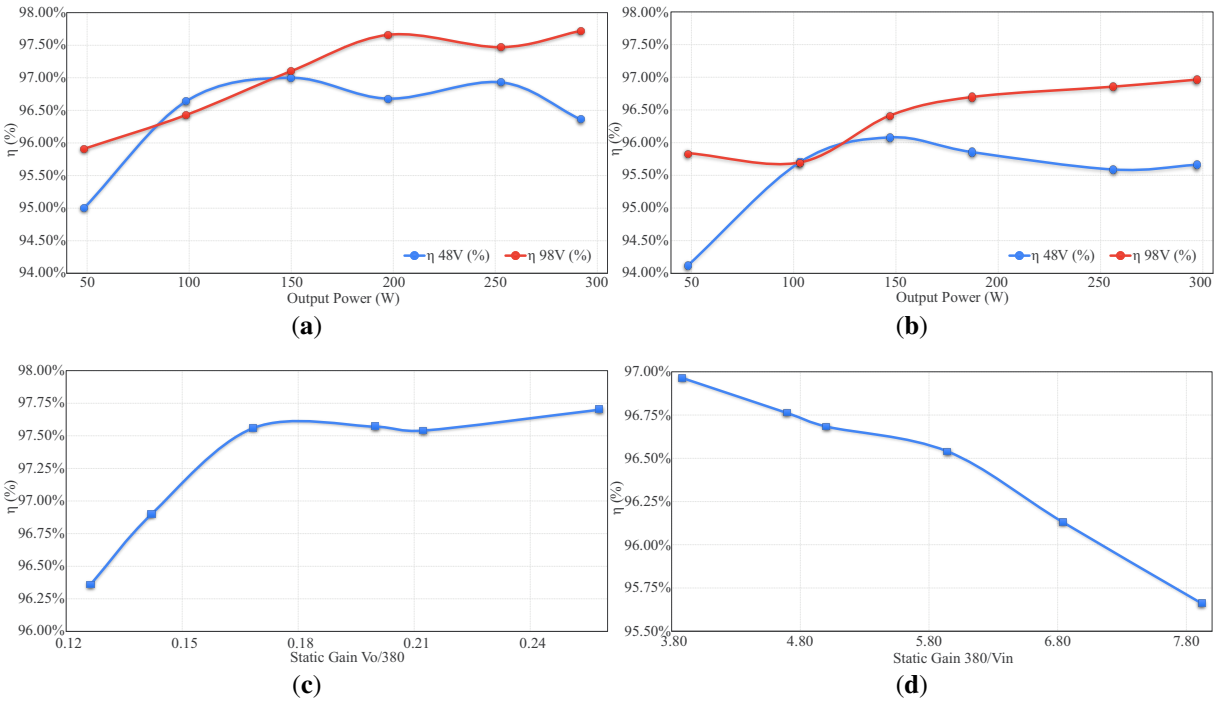


Figure 16. Converter efficiency: (**a**) Step-down for different loads. blue curve from 380 to 48 V. red curve from 380 to 98 V; (**b**) Step-up for different loads. blue curve from 48 to 380 V. red curve from 98 to 380 V; (**c**) step-down operation for different voltage gains at 300 W; (**d**) step-up operation for different voltage gains at 300 W.

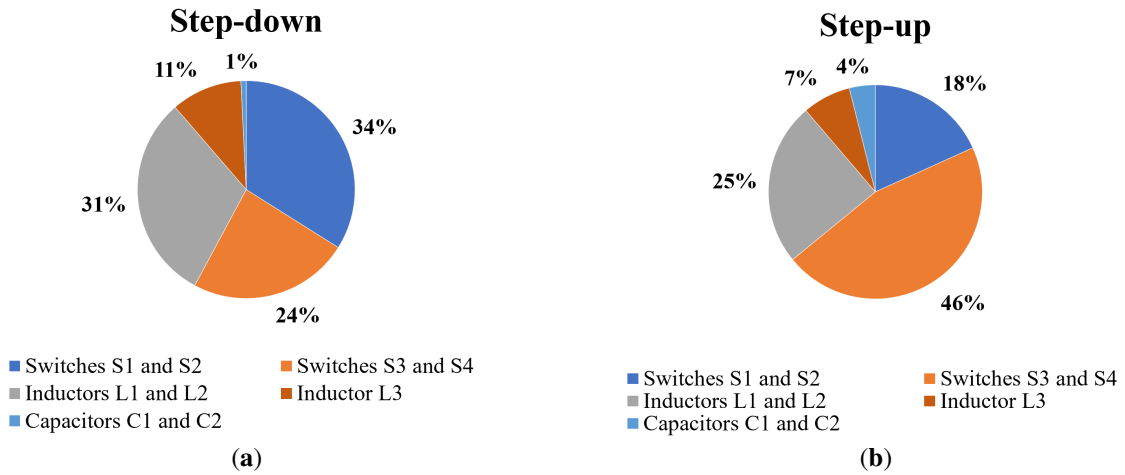


Figure 17. Loss distribution at rated power: (**a**) step-down operation; (**b**) step-up operation.

4.0.3. Controller Validation

To evaluate the proposed control strategy, experimental load-step tests were performed under low-voltage-side voltage and current regulation. Figures 18 and 19 show the low-side voltage V_2 and current I_2 for the respective control modes.

Figure 18 presents the response of the voltage controller to a load increasing from 57 W to 267 W, with the voltage reference maintained at $V_{2,\mathrm{ref}} = 48$ V. Following the load reduction, the output voltage exhibits an overshoot of approximately 8 V, corresponding to 16.7% of the reference value. The PI controller restores the output voltage to its reference, with a settling time of approximately 60 ms.

Figure 19 presents the response of the current controller to two successive changes in load resistance, with the current reference maintained at $I_{2,\mathrm{ref}} = 3.8$ A. Initially, the converter supplies a 13 Ω resistive load at approximately 49 V and 3.8 A, corresponding to an output power of approximately 186 W. The load resistance is then reduced to 8.7 Ω, causing the output current to rise momentarily to approximately 5.6 A. The controller restores the current to 3.8 A by reducing the output voltage to approximately 33 V, with a settling time of approximately 170 ms.

Subsequently, the load resistance is increased from 8.7 Ω to 13 Ω, producing a transient current undershoot of approximately 1.3 A relative to the reference. The controller restores the current to 3.8 A while the output voltage returns to approximately 49 V, with a settling time of approximately 200 ms. The change in steady-state voltage is expected because the controller regulates the output current while the load resistance changes.

These results demonstrate reference recovery following load disturbances for both control modes. Under voltage regulation, the controller maintains V_2 at its reference while the load current changes. Under current regulation, the controller maintains I_2 at its reference while the output voltage adjusts to the load resistance.

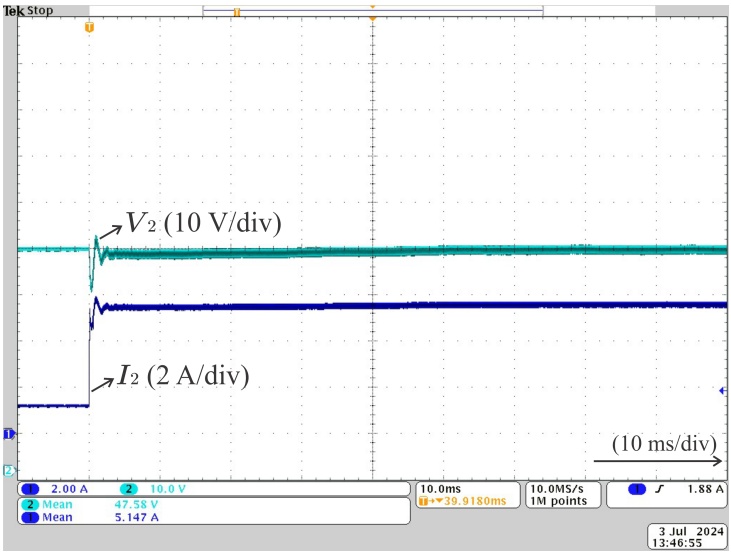


Figure 18. Experimental load-step response under low-voltage-side voltage regulation: load increasing from 57 W to 267 W with $V_{2,\mathrm{ref}} = 48$ V. Waveforms: low-side voltage V_2 and low-side current I_2.

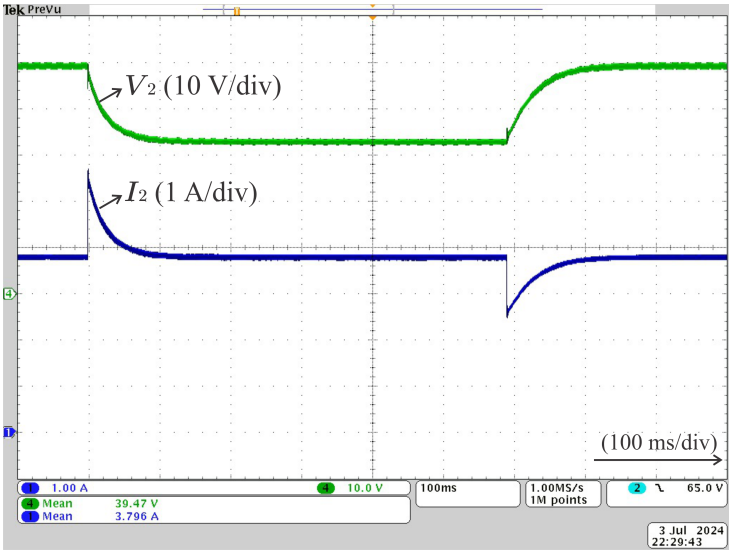


Figure 19. Experimental load-step response under low-voltage-side current regulation: load resistance changes from 13 Ω to 8.7 Ω and subsequently returns to 13 Ω, with $I_{2,\mathrm{ref}} = 3.8$ A. Waveforms: low-side voltage V_2 and low-side current I_2.

Similarly, closed-loop tests were performed with the converter operating in step-up mode, considering voltage and current regulation on the high-voltage side. Figures 20 and 21 show the high-side voltage V_1 and current I_1 for the respective control modes.

Figure 20 presents the response of the voltage controller to a load increase, with the voltage reference maintained at $V_{1,\mathrm{ref}} = 380$ V. The load is increased from approximately 150 W to 300 W, producing an instantaneous voltage undershoot of approximately 80 V, corresponding to 21% of the reference value. The controller restores the output voltage to its reference, with a settling time of approximately 45 ms.

Figure 21 presents the response of the current controller to two successive changes in load resistance, with the current reference maintained at $I_{1,\mathrm{ref}} = 420$ mA. Initially, the converter supplies a 667 Ω resistive load at approximately 280 V and 420 mA. The load resistance is then reduced to 500 Ω, corresponding to an increase in the load from approximately 150 W to 300 W. This load increase causes the output current to rise momentarily by approximately 160 mA. The controller restores the current to 420 mA by reducing the output voltage to approximately 210 V, with a settling time of approximately 300 ms.

Subsequently, the load resistance is increased from 500 Ω back to 667 Ω, producing a reduction in the output current. The controller restores the current to 420 mA by increasing the output voltage to approximately 280 V, with a settling time of approximately 300 ms. The change in steady-state voltage is expected because the controller regulates the output current while the load resistance changes.

These results demonstrate reference recovery following load disturbances for both control modes. Under voltage regulation, the controller maintains V_1 at its reference while the load current changes. Under current regulation, the controller maintains I_1 at its reference while the output voltage adjusts to the load resistance.

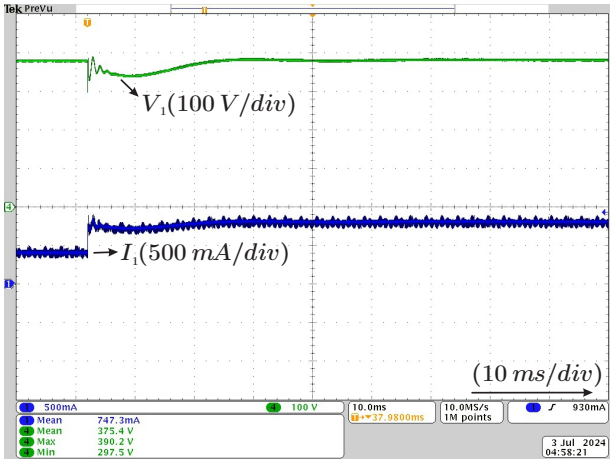


Figure 20. Experimental load-step response under high-voltage-side voltage regulation: load increasing from approximately 150 W to 300 W with $V_{1,\mathrm{ref}} = 380$ V. Waveforms: high-side voltage V_1 and high-side current I_1.

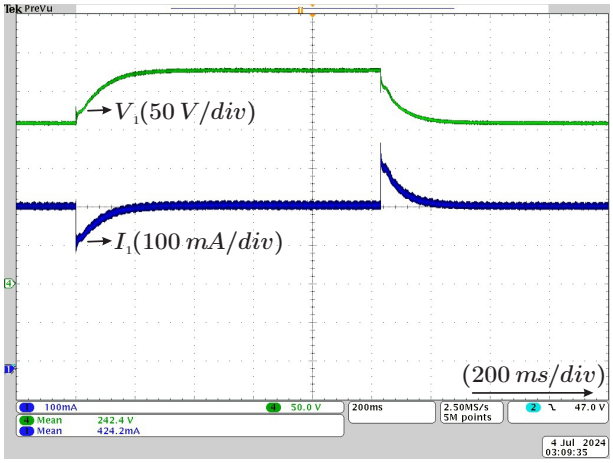


Figure 21. Experimental load-step response under high-voltage-side current regulation: load resistance changing from 667 Ω to 500 Ω, with $I_{1,\mathrm{ref}} = 420$ mA. Waveforms: high-side voltage V_1 and high-side current I_1.

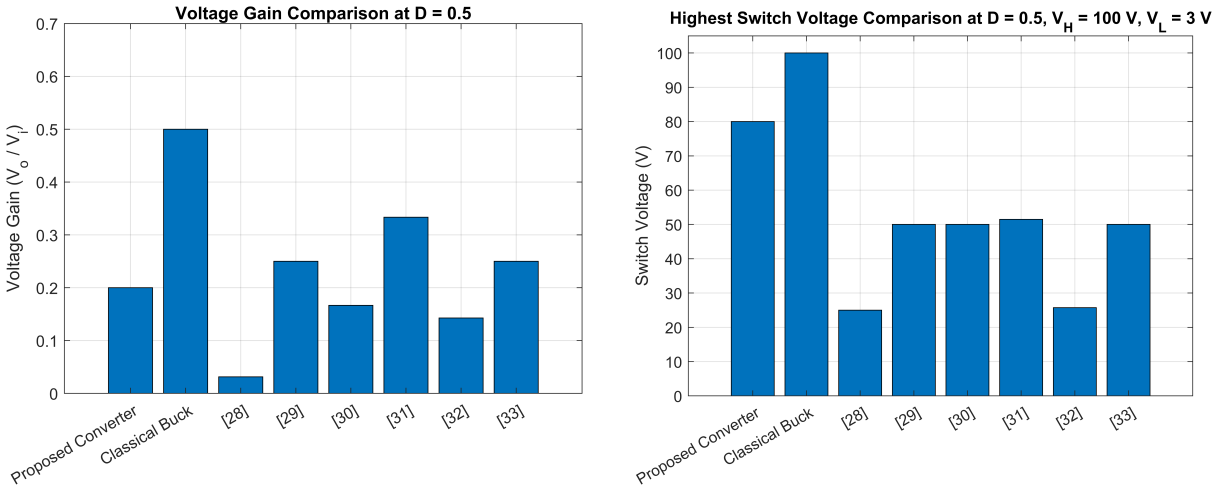
Buck and boost operation were experimentally validated separately. The small-signal models and load-step tests characterize the converter around the respective operating points, but do not establish its dynamic performance during power-flow reversal. The available laboratory setup lacked the controlled power-sourcing and power-absorption capabilities required for a reversal test. Therefore, seamless power-flow reversal is not demonstrated in this work, and dedicated dynamic analysis and experimental validation of this transition remain topics for future investigation.

5. Other Bidirectional Gain Cell Topologies and Comparison with the Developed Topology

The comparative analysis focuses on non-isolated DC–DC converters employing voltage-gain cells, particularly switched-capacitor structures, which provide a direct basis for assessing the proposed conversion mechanism. Although the DAB and its variants are established solutions for bidirectional power conversion, they provide galvanic isolation and voltage matching through a transformer, resulting in different design tradeoffs. Accordingly, this comparison evaluates the proposed topology within the non-isolated gain-cell-based category and does not imply superiority over DAB converters.

Only a limited number of bidirectional converters within this category have been reported for voltage conversion ratios comparable to that required between the 48 V and 380 V buses. Therefore, the analysis includes bidirectional converters operating at different voltage and power levels, as well as selected unidirectional high-conversion-ratio topologies whose circuit structures can potentially support bidirectional operation. The comparison considers static voltage gain, maximum switch-voltage stress, rated power, switching frequency, efficiency, and the numbers of passive components and semiconductor devices. Differences in operating conditions and implementation must be considered when interpreting the reported performance.

For example, the converter presented in [30] employs switched-capacitor cells to achieve a conversion from 48 V to 1 V. Although its circuit structure can support bidirectional operation, the reported experimental results refer to a 30-W unidirectional prototype employing 12 capacitors and 22 switches. In [27], a converter with a smaller number of components and higher efficiency was developed, but with lower gain and higher switch stress when compared to the proposed converter. Additionally, ref. [33] presents a converter with conversion from 48 V to 8 V; however, it exhibits lower efficiency and a higher number of components. Ref. [29] presents a converter with a rated power of 1 kW, 95% efficiency, and only one inductor in the topology; however, it presents a lower voltage gain, ref. [34] presents a converter with 400 V to 40-56 V with 96.1% efficiency, but with more switches and passive components and finally, ref. [28] also presents a converter with 400 V on the high side and 48 V on the low side, but with 92.8% peak efficiency and lower voltage gain for the same duty cycle. Table 6 summarizes the static voltage gains, maximum switch-voltage stresses expressed in terms of the high-side voltage V_1 or low-side voltage V_2, prototype voltage levels, rated powers, switching frequencies, reported efficiencies, and numbers of capacitors, switches, diodes, and inductors. From this, it can be verified that the proposed converter is able to maintain a good balance among gain, power, and maximum switch stress when compared to the other topologies, as can be seen in Figure 22a,b, where the gains of these topologies are compared for a duty cycle of 0.5 and the maximum semiconductor stress for a high side voltage of 100 V and low side voltage of 3 V. These operating conditions were selected to provide a common basis for comparison, ensuring that the voltage stress experienced by the semiconductor switches can be evaluated under equivalent conversion conditions across the different topologies.



(**a**) (**b**)

Figure 22. Comparison between the proposed topology and other bidirectional converters: (**a**) step-down voltage gain for $D = 0.5$; (**b**) maximum switch voltage stress for $V_1 = 100$ V, and $V_2 = 3$ V.

Table 6. Qualitative and quantitative comparison between the proposed topology and other bidirectional converters.

Topology	Step-Down Voltage Gain	Highest Switch Voltage	Low-Side Voltage	High-Side Voltage	Power	Switching Frequency	Efficiency at P_{nominal}	Number of Components			
								C	S	D	L
Proposed Converter	$\frac{D}{4-3D}$	$V_1\frac{2}{4-3D}$	48 V	380 V	300 W	50 kHz	96.3% †	3	4	0	3
Classical Buck	D	V_1	–	–	–	–	–	1	1	1	1
[30] *	$\frac{D}{16}$	$\frac{V_1}{4}$	1 V	48 V	30 W	80 kHz	90.39%	12	22	0	3
[27]	$\frac{D}{2}$	$\frac{V_1}{2}$	14 V	42 V	140 W	20–70 kHz	96.3%	3	4	0	1
[33] *	$\frac{V_1}{6}$	$\frac{V_1}{2}$	8 V	48 V	20 W	58 kHz	88%	5	5	5	2
[29] *	$\frac{D}{2-D}$	$\frac{V_1+V_2}{2}$	150 V	600 V	1 kW	70 kHz	95%	4	3	1	1
[34]	$\frac{D}{4-D}$	$\frac{V_1+V_2}{4}$	40–56 V	400 V	2 kW	60 kHz	96.1%	6	8	0	4
[28]	$\frac{D}{2}$	$\frac{V_1}{2}$	48 V	400 V	400 W	25 kHz	92.9%	2	5	0	3

* The results presented refer to the unidirectional version, although the topology can operate in a bidirectional manner. † The proposed converter efficiency is reported for buck operation at the nominal output power of 300 W (380 V to 48 V). Peak efficiencies are 97.0% in buck mode and 96.1% in boost mode, obtained at approximately 150 W and 136.3 W, respectively.

6. Conclusions

This paper addressed the limited availability of non-isolated bidirectional DC–DC converters capable of operating with the high conversion ratio required between 48 V and 380 V buses. A converter combining an active switched-inductor cell with an active switched-voltage-multiplier cell was proposed to provide step-down operation from 380 V to 48 V and step-up operation in the reverse power-flow direction.

The static voltage gains of the proposed converter were derived separately for buck and boost operation. This distinction is particularly important in bidirectional converters because the voltage gain, duty-cycle definition, component stresses, port characteristics, and dynamic behavior may differ according to the power-flow direction. Representative switched-inductor and voltage-multiplier cells were therefore revisited under bidirectional operation, and their corresponding boost and buck gains were established and compared together with their required numbers of passive elements and controllable switches. This analysis provides a consistent basis for evaluating gain-cell-based topologies in both power-flow directions.

A 300 W prototype operating between 380 V and 48 V validated the theoretical analysis, bidirectional power flow, and voltage and current controllers under open- and closed-loop conditions. Peak efficiencies of 97.0% in buck mode and 96.1% in boost mode were achieved. The literature review further highlighted the limited number of directly comparable high-conversion-ratio bidirectional converters. Despite differences in voltage levels, rated power, and operating direction among the available references, the comparative analysis showed that the proposed converter provides a favorable balance among bidirectional voltage gain, semiconductor voltage stress, efficiency, and component count. Future investigations may extend this analysis to isolated converters and gain cells based on coupled inductors.

By comparing the proposed converter with similar ones reported in the literature, a favorable tradeoff among voltage gain, efficiency, semiconductor stresses, the number of switches, capacitors, and inductors, in addition to having the capability of bidirectional operation is verified.

7. Biographies of the Authors



Tiago Peron Metzger was born in Balneário Camboriú, Brazil, in 2000. He received the B.Sc. and M.Sc. degrees in Electrical Engineering from the Federal University of Santa Catarina, Brazil, in 2024 and 2026, respectively. He is currently pursuing the Ph.D. degree in Electrical Engineering at the same institution. His main research interests include power electronics and energy storage systems, with experience in high-gain DC–DC converters, battery spectroscopy, battery monitoring and management systems (BMS), uninterruptible power supply (UPS) platforms, and three-phase inverters. His research activities involve modeling, control, and instrumentation applied to power electronic systems and batteries.



Guilherme André Tomasi Bauer received his B.Sc. (2008) and M.Sc. (2025) degrees in Electrical Engineering from the Federal University of Santa Catarina (UFSC), Brazil, with a focus on power electronics. From 2009 to 2021, he worked at Companhia Estadual de Energia Elétrica (CEEE) on electromechanical design and protection of power systems for high-voltage substations. Since 2021, he has been with Empresa Brasileira de Serviços Hospitalares (EBSERH), where he is responsible for electrical maintenance and engineering projects in hospital facilities.



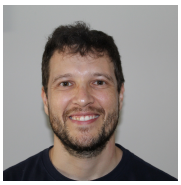
Bruno Benedetti was born in Londrina, PR, Brazil. He is currently pursuing the B.Sc. degree in Electrical Engineering at the Federal University of Santa Catarina (UFSC) and is an undergraduate research fellow at the Institute of Power Electronics (INEP/UFSC).



Luis Henrique Demeneck Sismeiro was born in Campo Grande, Mato Grosso do Sul, Brazil, in 2001. He received the B.Sc. degree in Electrical Engineering from the Federal University of Santa Catarina (UFSC), Florianópolis, Brazil, in 2025. He is currently pursuing the M.Sc. degree in Electrical Engineering, with emphasis on Power Electronics, at the Power Electronics Institute (INEP), UFSC. From 2024 to 2025, he was an intern with WEG, working in research and development activities related to motor drives and controls. His research interests include high-gain DC–DC converters, power converter topologies, digital control, PCB design, battery management systems, and electric powertrain applications.



Mateus Nava Mezaroba (S'19-M'26) was born in Jacutinga, Rio Grande do Sul, Brazil, in 1995. He received the B.Sc. degree in electrical engineering in 2018 from the Integrated Regional University of Alto Uruguai and Missions (URI), Erechim, Brazil. He received the M.Sc. and Ph.D. degrees in electrical engineering from the Federal University of Santa Catarina (UFSC), Florianópolis, Brazil, in 2021 and 2026, respectively. He is currently a postdoctoral researcher at the Power Electronics Institute (INEP), UFSC. Dr. Mezaroba is a member of the Brazilian Power Electronics Association (SOBRAEP), IEEE Power Electronics Society (PELS), IEEE Industry Applications Society (IAS), and IEEE Industrial Electronics Society (IES). His research interests include power electronics applied to renewable energy sources, grid-connected systems, and battery chargers.



Neilor Colombo Dal Pont was born in Criciúma, Santa Catarina, Brazil, in 1989. He received his B.Sc., M.Sc., and Ph.D. degrees in Electrical Engineering in 2015, 2017, and 2022, respectively, from the Federal University of Santa Catarina (UFSC), Florianópolis, where he was affiliated with the Department of Electrical and Electronic Engineering and the Power Electronics Institute. He is currently an electrical engineer at UFSC. His research interests focus on switched-capacitor converters, inverters, high-gain step-up and step-down DC–DC converters, resonant converters, and grid-connected systems.



Antonio Luiz Schalata Pacheco received the B.Sc. degree in mathematics, the M.Sc. degree in scientific and industrial metrology, and the Dr.Eng. degree in mechanical engineering from the Federal University of Santa Catarina (UFSC), Florianópolis, Brazil, in 2003, 2007, and 2015, respectively. He is a Researcher at the Institute of Power Electronics, UFSC. His main research interests include applied artificial intelligence, automation of tests, and development of measurement systems.



Jéssika Melo de Andrade was born in Florianópolis, Brazil, in July 1994, graduated in Electronic Systems at the Federal Institute of Santa Catarina (IFSC), Florianópolis, in 2015. She received the M.Sc. and Ph.D. degrees in Electrical Engineering from the Federal University of Santa Catarina (UFSC), Florianópolis, in 2018 and 2022, respectively. She is currently a Professor with the Department of Mobility Engineering (EMB) at the UFSC and a member of Brazilian Power Electronics Association (SOBRAEP). Her interests include high gain dc–dc converters, modeling and control applied to power electronics, converters/inverters with gain cells, renewable energy and related areas.



Telles Brunelli Lazzarin (S'09-M'12-SM'18) was born in Criciúma, Santa Catarina State, Brazil, in 1979. He received the B.Sc., M.Sc., and Ph.D. degrees in electrical engineering from the Federal University of Santa Catarina (UFSC), Florianópolis, Brazil, in 2004, 2006, and 2010, respectively. He is currently an Associate Professor with the Department of Electronic and Electrical Engineering (EEL) at UFSC. In 2006, he worked with industry, including R&D activities at WEG Motor Drives & Controls, Brazil. He was a Postdoctoral Fellow at UFSC, Florianópolis, Brazil, in 2011 and a Visiting Researcher at Northeastern University, Boston, USA, from 2017 to 2018. Dr. Lazzarin is a member of the Brazilian Power Electronics Association (SOBRAEP), IEEE Power Electronics Society (PELS), IEEE Industry Applications Society (IAS), and IEEE Industrial Electronics Society (IES). He has been an Associate Editor for the Brazilian Power Electronics Journal and IEEE Open Journal of Power Electronics (OJ-PEL) since 2020.

Author Contributions

T.P.M.: Coordinated the development of the converter and testing as well as writing reviewing and editing the paper; G.B.: Developed the static and dynamic analysis of the converter as well as the controller; B.B.: Testing of the converter; L.H.D.S.: Testing of the converter; M.N.M.: Writing, reviewing and editing the paper; N.C.D.P.: Testing of the converter; A.L.S.P.: Development and fabrication of the PCB; J.M.d.A.: supervision; T.B.L.: supervision. All authors have read and agreed to the published version

Funding

This research received no external funding.

Institutional Review Board Statement

Not applicable.

Informed Consent Statement

Not applicable.

Data Availability Statement

Data are contained within the article.

Acknowledgments

The authors acknowledge the financial support provided by the Fundação de Amparo à Pesquisa e Inovação do Estado de Santa Catarina (FAPESC, 2024TR002260) and the National Council for Scientific and Technological Development (CNPq) through the National Institute of Science and Technology in Power Electronics: Developing Technologies for a Sustainable Energy Transition (INCT EPTech), Grant 408822/2024-4.

Conflicts of Interest

The authors declare no conflict of interest.

Use of AI and AI-Assisted Technologies

No AI tools were utilized for this paper.

References

1. Campbell, K.; Diffley, J.; Flanagan, B.; et al. The 5G Economy: How 5G Technology Will Contribute to the Global Economy. 2017. Available online: https://www.qualcomm.com/media/documents/files/ihs-5g-economic-impact-study.pdf (accessed on 8 May 2026).
2. Milan, A.; Sahu, R.; Sandhu, J.K. Impact of AI on Social Marketing and its Usage in Social Media: A Review Analysis. In Proceedings of the 2023 International Conference on Circuit Power and Computing Technologies (ICCPCT), Kollam, India, 10–11 August 2023; pp. 1749–1754. https://doi.org/10.1109/iccpct58313.2023.10245676.
3. Katal, A.; Dahiya, S.; Choudhury, T. Energy efficiency in cloud computing data centers: a survey on software technologies. *Clust. Comput.* **2023**, *26*, 1845–1875. https://doi.org/10.1007/s10586-022-03713-0.
4. Shehabi, A.; Smith, S.J.; Masanet, E.; et al. Data center growth in the United States: decoupling the demand for services from electricity use. *Environ. Res. Lett.* **2018**, *13*, 124030. https://doi.org/10.1088/1748-9326/aaec9c.
5. Mendonça, S.; Damásio, B.; Charlita de Freitas, L.; et al. The rise of 5G technologies and systems: A quantitative analysis of knowledge production. *Telecommun. Policy* **2022**, *46*, 102327. https://doi.org/10.1016/j.telpol.2022.102327.
6. IEA. Energy and AI. 2025. Available online: https://www.iea.org/reports/energy-and-ai (accessed on 21 April 2026).
7. Chen, Y.; Shi, K.; Chen, M.; et al. Data Center Power Supply Systems: From Grid Edge to Point-of-Load. *IEEE J. Emerg. Sel. Top. Power Electron.* **2023**, *11*, 2441–2456. https://doi.org/10.1109/jestpe.2022.3229063.
8. Li, X.; Jiang, S. Google 48 V Rack Adaptation and Onboard Power Technology Update. In Proceedings of the OCP Global Summit, San Jose, CA, USA, 14–15 March 2019.
9. Erickson, R.W.; Maksimović, D. *Fundamentals of Power Electronics*, 2nd ed.; Springer: Boston, MA, USA, 2001. https://doi.org/10.1007/b100747.
10. Texas Instruments. TPS84621 2.95-V to 14.5-V input, 6-A Synchronous Buck, Integrated Power Solution. 2012. Available online: http://www.ti.com/lit/ds/symlink/tps84621.pdf (accessed on 01 June 2026).
11. Fei, C.; Gadelrab, R.; Li, Q.; et al. High-Frequency Three-Phase Interleaved LLC Resonant Converter with GaN Devices and Integrated Planar Magnetics. *IEEE J. Emerg. Sel. Top. Power Electron.* **2019**, *7*, 653–663. https://doi.org/10.1109/jestpe.2019.2891317.
12. Knabben, G.C.; Schäfer, J.; Kolar, J.W.; et al. Wide-Input-Voltage-Range 3 kW DC–DC Converter with Hybrid LLC & Boundary/Discontinuous Mode Control. In Proceedings of the 2020 IEEE Applied Power Electronics Conference and Exposition (APEC), New Orleans, LA, USA, 15–19 March 2020; pp. 1359–1366. https://doi.org/10.1109/apec39645.2020.9124410.
13. Yu, R.; Chen, T.; Liu, P.; et al. A 3-D Winding Structure for Planar Transformers and Its Applications to LLC Resonant Converters. *IEEE J. Emerg. Sel. Top. Power Electron.* **2021**, *9*, 6232–6247. https://doi.org/10.1109/jestpe.2021.3052712.
14. Gadelrab, R.; Nabih, A.; Lee, F.C.; et al. LLC Resonant Converter with 99% Efficiency for Data Center Server. In Proceedings of the 2021 IEEE Applied Power Electronics Conference and Exposition (APEC), Phoenix, AZ, USA, 14–17 June 2021; pp. 310–319. https://doi.org/10.1109/apec42165.2021.9487423.
15. Nabih, A.; Li, Q. Low-Profile and High-Efficiency 3 kW 400 V-48 V LLC Converter with a Matrix of Four Transformers and Inductors for 48 V Power Architecture for Data Centers. In Proceedings of the 2021 IEEE Energy Conversion Congress and Exposition (ECCE), Vancouver, BC, Canada, 10–14 October 2021; pp. 1813–1819. https://doi.org/10.1109/ecce47101.2021.9595881.
16. Ranjram, M.K.; Perreault, D.J. A 380-12 V, 1 kW, 1 MHz Converter Using a Miniaturized Split-Phase, Fractional Turn Planar Transformer. *IEEE Trans. Power Electron.* **2022**, *37*, 1666–1681. https://doi.org/10.1109/tpel.2021.3103434.
17. Pan, S.; Wang, C.; Jain, P. Structure and Implementation of a Hybrid 48V/380V DC UPS for IT Datacenters. In Proceedings of the 2018 IEEE Energy Conversion Congress and Exposition (ECCE), Portland, OR, USA, 23–27 September 2018; pp. 3851–3856. https://doi.org/10.1109/ecce.2018.8557425.
18. Forouzesh, M.; Siwakoti, Y.P.; Gorji, S.A.; et al. Step-Up DC–DC Converters: A Comprehensive Review of Voltage-Boosting Techniques, Topologies, and Applications. *IEEE Trans. Power Electron.* **2017**, *32*, 9143–9178. https://doi.org/10.1109/tpel.2017.2652318.
19. Yang, L.S.; Liang, T.J.; Chen, J.F. Transformerless DC–DC Converters With High Step-Up Voltage Gain. *IEEE Trans. Ind. Electron.* **2009**, *56*, 3144–3152. https://doi.org/10.1109/tie.2009.2022512.
20. Tang, Y.; Fu, D.; Wang, T.; et al. Hybrid Switched-Inductor Converters for High Step-Up Conversion. *IEEE Trans. Ind. Electron.* **2015**, *62*, 1480–1490. https://doi.org/10.1109/tie.2014.2364797.
21. Ismail, E.H.; Al-Saffar, M.A.; Sabzali, A.J.; et al. A Family of Single-Switch PWM Converters With High Step-Up Conversion Ratio. *IEEE Trans. Circuits Syst. I Regul. Pap.* **2008**, *55*, 1159–1171. https://doi.org/10.1109/tcsi.2008.916427.

22. Prudente, M.; Pfitscher, L.; Gules, R. A Boost Converter with Voltage Multiplier Cells. In Proceedings of the 2005 IEEE 36th Power Electronics Specialists Conference, Recife, Brazil, 12–16 June 2005; pp. 2716–2721. https://doi.org/10.1109/pesc.2005.1582017.
23. Salvador, M.A.; de Andrade, J.M.; Lazzarin, T.B.; et al. Nonisolated High-Step-Up DC–DC Converter Derived from Switched-Inductors and Switched-Capacitors. *IEEE Trans. Ind. Electron.* **2020**, *67*, 8506–8516. https://doi.org/10.1109/tie.2019.2949535.
24. Sarani, S.; Liang, X. Non-Isolated High Voltage Gain Bidirectional DC–DC Converters: A Review. In Proceedings of the 2024 IEEE Industry Applications Society Annual Meeting (IAS), Phoenix, AZ, USA, 20–24 October 2024; pp. 1–7. https://doi.org/10.1109/ias55788.2024.11023749.
25. Wenk, M.; Zimann, F.J.; Mayer, R.; et al. Dynamic Modeling and Experimental Validation of a Non-Isolated Bidirectional DC–DC Converter for Control-Oriented Design. *Eletrônica Potência* **2026**, *31*, e202614. https://doi.org/10.18618/rep.e202614.
26. Axelrod, B.; Berkovich, Y.; Ioinovici, A. Switched-Capacitor/Switched-Inductor Structures for Getting Transformerless Hybrid DC–DC PWM Converters. *IEEE Trans. Circuits Syst. I Regul. Pap.* **2008**, *55*, 687–696. https://doi.org/10.1109/tcsi.2008.916403.
27. Flores Cortez, D.; Waltrich, G.; Fraigneaud, J.; et al. DC–DC Converter for Dual-Voltage Automotive Systems Based on Bidirectional Hybrid Switched-Capacitor Architectures. *IEEE Trans. Ind. Electron.* **2015**, *62*, 3296–3304. https://doi.org/10.1109/tie.2014.2350454.
28. Chen, J.; Wang, C.; Li, J.; et al. A nonisolated three-level bidirectional DC–DC converter. In Proceedings of the 2018 IEEE Applied Power Electronics Conference and Exposition (APEC), San Antonio, TX, USA, 4–8 March 2018; pp. 1566–1570. https://doi.org/10.1109/apec.2018.8341225.
29. Vecchia, M.D.; de Andrade, J.M.; Dal Pont, N.C.; et al. Proposal, Analysis and Experimental Verification of Nonisolated DC–DC Converters Conceived from an Active Switched-Capacitor Commutation Cell. *Eletrônica Potência* **2019**, *24*, 403–412. https://doi.org/10.18618/rep.2019.4.0031.
30. Dal Pont, N.C.; De Andrade, J.M.; Bharatiraja, C.; et al. 48 V to 1 V DC–DC Converter Based on Cascade/Ladder Connected Switched Capacitor Cells. *Eletrônica Potência* **2025**, *30*, e202525. https://doi.org/10.18618/rep.e202525.
31. Silva, G.V.; de Andrade, J.M.; Coelho, R.F.; et al. Switched-Capacitor Differential Boost Inverter: Design, Modeling, and Control. *IEEE Trans. Ind. Electron.* **2020**, *67*, 5421–5431. https://doi.org/10.1109/tie.2019.2931258.
32. Vecchia, M.D.; Salvador, M.A.; Lazzarin, T.B. Hybrid Nonisolated DC–DC Converters Derived From a Passive Switched-Capacitor Cell. *IEEE Trans. Power Electron.* **2018**, *33*, 3157–3168. https://doi.org/10.1109/tpel.2017.2703912.
33. Folmer, S.; Kosakowski, M.; Stala, R. 48-V Input DC–DC High Step-Down Converter in GaN-Based Design. *IEEE Access* **2022**, *10*, 115958–115973. https://doi.org/10.1109/access.2022.3218309.
34. Rahman, S.; Ayaz, M.A.; Khan, I.A. Review of Non-Isolated DC/DC Converters for Application in Data Center Power Delivery. In Proceedings of the 2024 4th International Conference on Smart Grid and Renewable Energy (SGRE), Doha, Qatar, 8–10 January 2024; pp. 1–6. https://doi.org/10.1109/sgre59715.2024.10428839.